

Simulating Nanoscale Imaging of Plasmonic Excitations and Cancer Cells under Near-field Nanoscopy

Derek Chen

Simulating Nanoscale Imaging of Plasmonic Excitations and Cancer Cells under Near-field Nanoscopy

Abstract

Scattering-type scanning near-field optical microscopy (s-SNOM) is an advanced optical method to achieve fine resolution at the nanoscale. s-SNOM provides novel opportunities to study a variety of materials, such as strongly correlated quantum materials (SCQMs), and processes such as plasmonic excitations in gold nanoparticles at infrared and terahertz frequencies. Studying the optical properties of advanced materials, including the plasmonic resonances of gold particles, as well as the optical responses of normal and cancerous human cells, provides fundamental insights for the application of nano-imaging techniques to the medical field, such as in cancer diagnosis. In this work, the discrete dipole approximation is implemented to simulate s-SNOM imaging and spectroscopy. Results from s-SNOM spectroscopy simulations of silicon carbide (SiC) and silicon dioxide (SiO₂) are presented, which have good agreement with previous theoretical, numerical, and experimental results. 2-dimensional imaging of gold nanoparticles and hexagonal boron nitride (hBN) are shown to accurately display plasmonic and polaritonic patterns. In addition, simultaneous imaging of normal human and breast cancer cells are shown to accurately display expected optical contrasts. The dipole approximation is thus shown to have novel applications for a variety of optical applications, including the imaging of plasmonic and polaritonic excitations as well as cancer cells, with implications for future imaging techniques using plasmonic field enhancement as well as optical cancer diagnosis.

Simulating Nanoscale Imaging of Plasmonic Excitations and Cancer Cells under Near-field Nanoscopy

1. Introduction

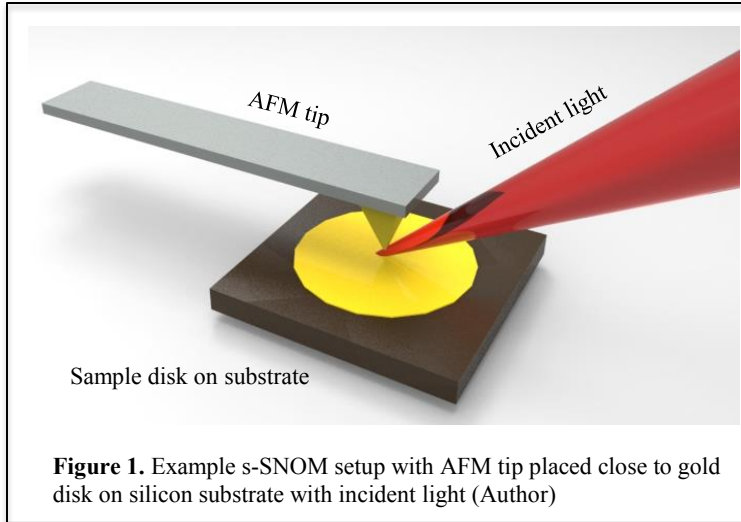
1.1 Rationale

Novel microscopy imaging methods within the terahertz (THz) frequency range, falling between microwave and infrared from .1 to 10 THz^{1,2}, provide novel opportunities to image biological cells, such as cancer cells^{1,2,3,4,5}, as well as physical phenomena, such as plasmonic modes and polaritonic excitations^{1,6,7,8,9,10}. Frequencies within the THz range have low photon energy^{1,3}; as a result, cells are not damaged in this non-invasive process of imaging^{1,3}. In addition, THz can be used to highlight optical contrasts and provide higher resolutions than those of higher-energy imaging methods, such as x-rays³.

Furthermore, THz has been shown to be applicable to novel near-field imaging methods, including scattering-type scanning near-field optical microscopy (s-SNOM)¹. s-SNOM has been applied to the direct imaging of polaritons and plasmonic modes in various materials, such as gold and hexagonal boron nitride (hBN)^{1,6,7,8,9,10}, and has shown spatial resolution down to 10 nm, regardless of the incident wavelength¹. Because s-SNOM is desired for investigating the optical properties of materials at the nanoscale, particularly strongly correlated quantum materials (SCQMs)^{1,11}, more accurate models for s-SNOM are thus needed in order to precisely depict experimental expectations and results, especially in the THz regime, in which imaging currently faces experimental challenges such as a high signal-to-noise ratio in imaging¹. Due to the presence of the s-SNOM probe, experimentally determined optical contrasts are difficult to quantitatively interpret, making accurate models a necessity¹.

Biomedical fields depend on contrasts in optical imaging in cancer diagnosis³. Cancer is responsible for 25% of deaths in the United States³, and preceded only by heart disease in the prevalence of the lives it takes³; since effective and efficient diagnosis is critical to cancer treatment, precise imaging of cancerous cells is imperative for cancer treatment, as such imaging is necessary for diagnosis³. THz imaging, in conjunction with s-SNOM, may provide novel opportunities of biomedical imaging. Such THz imaging would be non-invasive, and could offer high image resolution, which would make it superior to existing methods, such as x-rays and MRIs³.

This study had several aims: 1) to create a robust simulation method for microscopy and spectroscopy; and 2) to demonstrate the potential of s-SNOM for application in the both the physical and biomedical regimes. These two aims would ultimately improve s-SNOM and THz imaging by providing more a more accurate method for verification of experimental results and for prediction of future results, which would allow for possible novel approaches to nanoscale imaging of materials and cancer diagnosis.



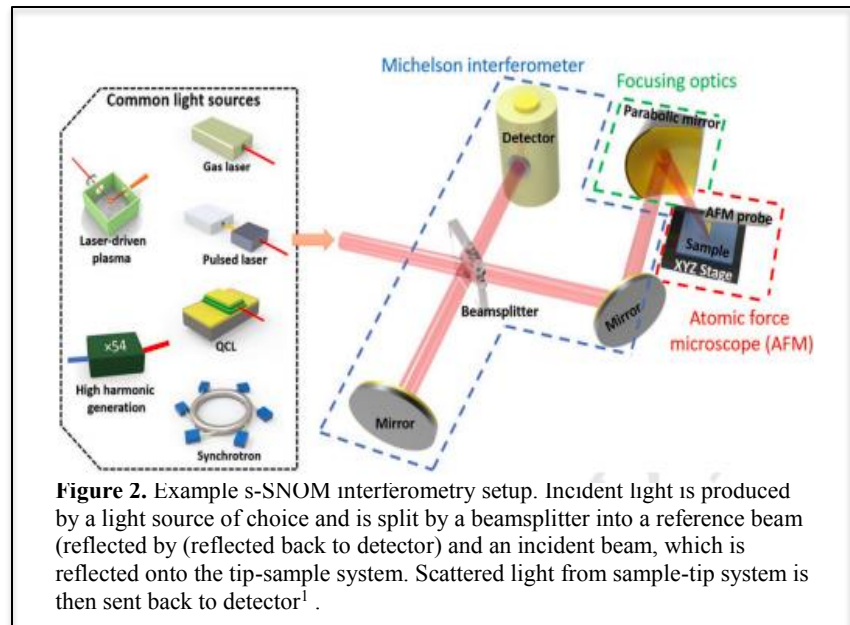
1.2 Background

Scattering-type scanning near-field optical microscopy (s-SNOM)

In conventional optics, signals are measured in the far-field regime, where images are produced from light propagating from a sample¹. In near-field imaging methods, images are produced from non-propagating

(‘near-field’) evanescent waves produced by the sample, thereby allowing certain optical properties of samples to be accessed, notably the dielectric constant of the sample, which determines the scattered response of the sample to light¹.

In s-SNOM, this near-field is accessed through an atomic force microscope (AFM) tip placed close to the sample¹. This tip interacts with the sample, allowing for previously non-propagating fields to be enhanced and propagated into the far-field regime¹ (**Figure 1**); this signal can then be demodulated through the usage of a Fourier series to access the desired near-field signal¹. A traditional s-SNOM system employs a setup similar to a Michelson interferometer (**Figure 2**), in which incident light is divided into reference and probe arms, both received by a detector for demodulation¹. A light source



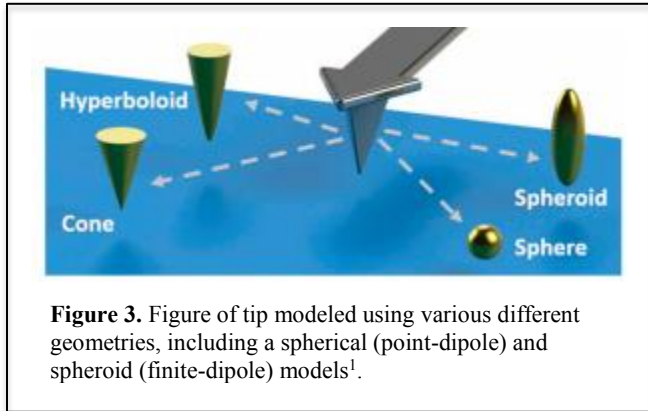
is used to provide incident light, typically in the infrared or visible regimes^{1,12}. Novel s-SNOM systems seek to operate in the THz regime and at cryogenic temperatures¹; THz imaging is desired for its

applications to biological cells, phonons, and superconductors, while cryo-s-SNOM is desired for observing low-temperature phenomenon¹.

Currently, a major limiting factor of s-SNOM lies in the methods to model it¹. Traditionally, analytical models and numerical solvers have been applied to model s-SNOM systems; however, these methods are limited in various ways: analytical models are computationally expensive and require samples to be perfectly homogeneous, while numerical solvers are time consuming and are particular to a given sample system^{1,12}. In this work, the difficulties presented to both of these methods are resolved through the semi-analytical discrete dipole approximation (DDA). In this study, this method is presented to accurately reproduce experimental s-SNOM results, especially for polaritonic and plasmonic patterns.

Analytical Models

Several analytical models have been produced to better understand experimentally produced results^{1,13,14}. Analytical models are necessary for understanding tip-sample interactions in s-SNOM, which are critical to understanding experimental results^{1,14}.



The most basic analytical model of s-SNOM is the point-dipole model (**Figure 3**), which approximates the probing tip as a single spherical dipole^{1,14}. More complex models include the finite-dipole model¹³, lightning rod model¹, and the conformal mapping method¹. Analytical models have been limited by their

computational complexity as well as the difficulty posed by inhomogeneous samples, which are difficult to treat analytically².

Alternative tools for simulating s-SNOM systems include numerical solvers, such as CST Microwave Studio^{1,12}. Numerical solvers are able to account for particular solutions for a given system. Issues with numerical solvers include lengthy computation time, as well as a loss of generality of the solution^{1,12}.

Imaging of Plasmonic Modes and Polaritons

s-SNOM imaging has been used to image plasmonic modes in different materials, particularly in gold nanoparticles^{9,10}; plasmonic modes in gold nanoparticles were imaged using s-SNOM by Hillenbrand¹⁰ and Garcia-Etxarri⁹. s-SNOM imaging has additionally been used to image surface

polaritons⁸ and phonon polaritons⁷ in hBN. Accurate imaging and simulations are required to rigorously study these responses. In this study, I implemented a method to systematically and accurately reproduce s-SNOM imaging of plasmonic modes and polaritonic responses.

1.3 Objectives

The objectives of this work were two-fold: 1) to create a robust method for s-SNOM imaging applicable in the THz regime for simulating experimental results; and 2) to demonstrate the applicability of this method for the imaging of plasmonic and polaritonic modes and cancer diagnosis. In order to achieve these goals, the discrete dipole approximation (DDA) was adapted to s-SNOM for simulation; simulations of plasmonic modes in gold nanoparticles and optical contrasts between cancerous and non-cancerous cells are revealed through near-field THz simulations.

2. Methodology

**Unless otherwise stated, all methods were conducted by the Author.*

2.1 Discrete Dipole Approximation

The discrete dipole approximation (DDA) was used to create a general, yet practical, simulation method for the imaging of normal and cancerous human cells, plasmonic modes in gold, and polaritonic modes in hBN under s-SNOM.

Purcell and Pennypacker were the first to develop DDA; they first employed DDA to study light scattered by interstellar dust grains in 1973¹⁵. Their work was followed by and expanded upon by Draine and Flatau^{16,17,18}. DDA has since been employed in many other systems; for example, DDA has been applied to study coupling of samples with evanescent waves in atomic force microscopy (AFM)¹⁹, and has also been applied to study scanning near-field microscopy using total internal reflection²⁰. However, the application of the DDA to s-SNOM, and particularly for simulation of cells and plasmonic modes, has yet to be accomplished. I thus created a Python implementation of DDA for s-SNOM based on existing source code²¹ and applied this implementation to simulate images of various samples.

The existing source code for DDA that I built upon relied upon formalism established by Draine and Flatau^{16,17,21}, which is presented here.

DDA models objects as collections of interacting spherical dipoles^{16,17,18}. In order for DDA to be applied, two validity criteria must be satisfied: firstly, spacing between the dipoles must be small in relation to the wavelength of the light introduced, governed by the equation

$$|m|kd \leq 1 \text{ (Equation 1)}^{17};$$

where d is the lattice spacing, k is the wavenumber, and m is the refractive index of the material¹⁷. I supposed this criteria to be satisfied, as the lattice spacing used in simulation was at the nanoscale, significantly smaller than the wavelengths of the mid-infrared frequencies used for s-SNOM. The second criteria required that the number of spheres used to approximate the sample needed to be large enough to accurately represent the sample; as no formal formulation existed for this criteria¹⁷, I based the validity of this criteria on the accuracy of the simulation in producing objects under s-SNOM, detailed in Section 2.2.

Once these criteria were satisfied, the scattering of light was simplified to a system of linear equations describing the polarizations of each individual sphere, which were represented as a system of matrix equations. These systems were solved through a Python implementation²¹ for the polarizations of each sphere in response to incident light, which in turn describe the scattering response to the incident light¹⁷. The scattered response can then be quantified and demodulated^{16,17,18}.

The extraction of a scattered response through DDA was as follows:

The aim of the DDA was to solve for the polarizations of each dipole j located at position \mathbf{r}_j , for N dipoles; this polarization was then used to solve for the scattered response of the system¹⁷. The polarization of each dipole j is described by

$$\mathbf{P}_j = a_j \mathbf{E}_j \text{ (Equation 2)}^{17},$$

where a_j is the polarizability of the dipole, described using the Clausius-Mossotti polarizability¹⁷:

$$a_j^{CM} = \frac{3d^3(\epsilon_j - 1)}{4\pi(\epsilon_j + 2)} \text{ (Equation 3)}^{17}$$

and \mathbf{E}_j is the resultant electric field acting on the dipole as a result of both the incident light and all the other dipoles:

$$\mathbf{E}_j = \mathbf{E}_{inc,j} - \sum_{k \neq j} A_{jk} \mathbf{P}_k \text{ (Equation 4)}^{17}$$

with $\mathbf{E}_{inc,j}$ describing the incident electric field, given by

$$\mathbf{E}_{inc,j} = \mathbf{E}_0 \exp(i\mathbf{k} \cdot \mathbf{r}_j - i\omega t) \text{ (Equation 5)}^{17}$$

and $-\sum_{k \neq j} A_{jk} \mathbf{P}_k$ is the electric field resulting from all other dipoles k ¹⁷. A_{jk} , a 3 x 3 matrix which describes the impact of dipole k on dipole j for all dipoles $j \neq k$, is defined by

$$A_{jk} = \frac{\exp(ikr_{jk})}{r_{jk}^3} \times (k^2(\hat{r}_{jk}\hat{r}_{jk} - 1_3) + \frac{ikr_{jk}-1}{r_{jk}^2}(3\hat{r}_{jk}\hat{r}_{jk} - 1_3)) \text{ (Equation 6)}^{17}$$

with $k = \omega/c$, $r_{jk} = |\mathbf{r}_j - \mathbf{r}_k|$ is the distance between the dipoles, $\hat{r}_{jk} = |\mathbf{r}_j - \mathbf{r}_k|/r_{jk}$ is the distance unit vector, and $\mathbf{1}_3$ is an identity matrix with dimensions identical to A_{jk} ¹⁷. The impact of the dipole's polarizability on itself can be described as $A_{jj} = \alpha_j^{-1}$, or the inverse polarizability of the dipole¹⁷. Equation 4 can thus be manipulated to give

$$\mathbf{E}_j + \sum_{k \neq j} A_{jk} P_k = \mathbf{E}_{\text{inc},j} \quad (\text{Equation 7})^{17}$$

the left hand side can thus be reduced to $\sum_{k=1}^N A_{jk} P_k$, yielding

$$\sum_{k=1}^N A_{jk} P_k = \mathbf{E}_{\text{inc},j} \quad (\text{Equation 8})^{17},$$

which defines a system of equations that can be solved for \mathbf{P}_j ¹⁷. This can be done with several methods, primarily iterative methods such as the complex-conjugate gradient method (CCG)^{17,18}. These iterative methods are able to solve equations for large numbers of dipoles, while also being computationally efficient¹⁸. The Python implementation used in this work made use of the SciPy Python library's biConjugate gradient stabilized method to solve this system of equations²¹.

The polarizabilities can then be used to solve for extinction and absorption cross sections, which are defined by the total power from the incident light and power absorbed, respectively¹⁵. This can then be used to solve for the scattered response of the system by calculating the scattering cross section, which can be expressed as

$$C_{\text{scat}} = C_{\text{ext}} - C_{\text{abs}} \quad (\text{Equation 9})^{17}$$

where

$$C_{\text{ext}} = \frac{4\pi k}{|E_0|^2} \sum_{j=1}^N \text{Im}(\mathbf{E}_{\text{inc},j}^* \cdot \mathbf{P}_j) \quad (\text{Equation 10})^{17}$$

and

$$C_{\text{abs}} = \frac{4\pi k}{|E_0|^2} \sum_{j=1}^N (\text{Im}(\mathbf{P}_j \cdot (\alpha_j^{-1})^* (\mathbf{P}_j)^*) - \frac{2}{3} k^3 |\mathbf{P}_j|^2) \quad (\text{Equation 11})^{17}.$$

This scattering response was calculated through the Python implementation²¹.

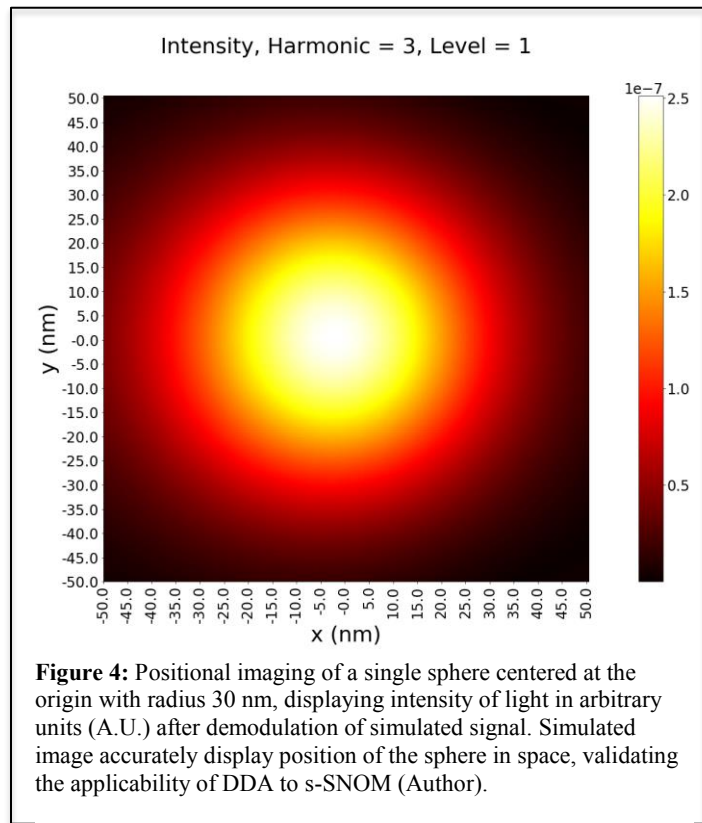
2.2 Python Implementation

Both tip and sample were modeled using interacting dipoles. Image spheres for all dipoles were used in order to model the effect of the substrate on the system. These spheres were reflected over the simulated surface of the substrate and simulated the substrate response to the system. Since the existing implementation of DDA has not yet been applied to s-SNOM, I adapted the existing source code²¹ to

simulate s-SNOM and apply this simulation to systems imaged by s-SNOM, such as plasmonic and polaritonic excitations, as well as biological samples. Previous unpublished work²² in the lab was used to simulate spheres in space and to produce a method for demodulating the calculated scattering response of the dipoles, retrieving the simulated signal produced by s-SNOM²². I then adapted the code to describe tips and samples of different geometries. In addition to this, I adapted the code to sweep over position in space, and applied the code to imaging cells and plasmonic modes.

Firstly, I adapted the code to accommodate for the tip geometry; this was accomplished by a Python function which approximated the s-SNOM tip as a series of n levels of spheres, with an $n \times n$ grid of spheres for each level. A tip with a single level would be a single sphere, approximating the tip as a point-dipole; a tip with two levels would have a first level with a single sphere and a second level with a two-by-two grid of spheres, located above the first level; and so on.

I then created Python functions to apply the code to simulate two-dimensional spatial images of s-SNOM imaging by creating two Python loops, which determined a spatial grid by cycling through all possible positions. I tested the validity of this geometric scan by running tests with a single sphere placed at the center of the grid. The sphere was shifted in position and run through the DDA code for its scattered response, which was later



demodulated for each position tested, in order to determine the intensity of the given point in space. The position of the sphere placed in space was accurately modeled (**Figure 4**). The simulated signal intensity was greatest in the location the sphere was centered; this demonstrated the validity of the approximation for spatial simulations, since the image of the sphere was accurately produced (**Figure 4**). Results were produced using a single point-dipole sphere to represent the tip.

Further tests for validity were performed with multiple spheres placed in various geometric patterns. Hexagonal and triangular samples were produced and simulated in space, and were accurately

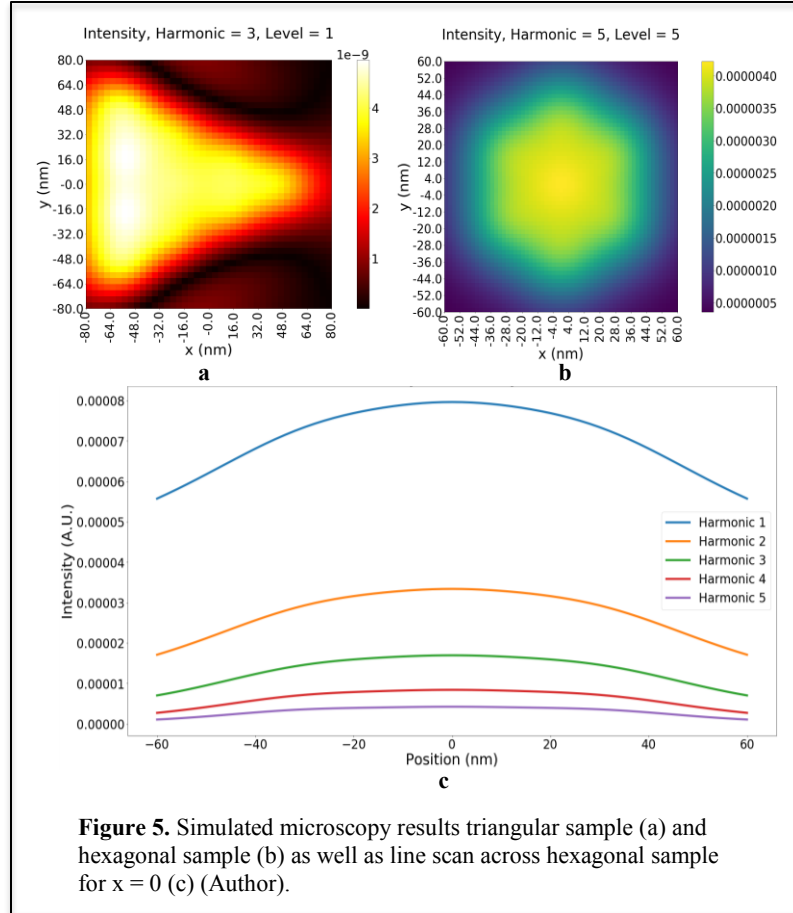


Figure 5. Simulated microscopy results triangular sample (a) and hexagonal sample (b) as well as line scan across hexagonal sample for $x = 0$ (c) (Author).

modeled (Figure 5a, 5b); triangular, hexagonal, and rectangular geometries were tested, in order to characterize experimental sample geometries. In all cases, the geometries were accurately modeled within space; this was confirmed with line scans across samples (Figure 5c), which confirmed that the areas of greatest optical intensity were aligned with the areas in which spheres were placed.

With validity tests for geometric scans completed, spectroscopy and microscopy scans were applied to the simulation method, with the aim of validating

the applicability of DDA to s-SNOM and various samples, including biological cells, as well as plasmonic and polaritonic excitations.

2.3 Spectroscopy and Microscopy Implementation

In order to further show the validity of the simulation method for s-SNOM and to apply the simulation method, dielectric parameters describing the optical responses of imaged samples were inputted to recreate previously simulated and experimental results. Dielectric information in the form of a dielectric constant ϵ or function $\epsilon(\omega)$ was thus used, changing the polarizability of the simulated dipoles to achieve the ultimate purpose of imaging. Typical s-SNOM experiments use a range of incident angles for incident light¹²; all simulations in this work were run at an incident angle of 45° for consistency.

Simulations were run for both spectroscopy and microscopy using s-SNOM. Spectroscopy simulations were run in comparison to previous numerical and analytical results for SiO₂¹² and SiC¹³.

Spectroscopy simulations for SiO₂ were modeled after experimental and numerical simulations¹², with $\epsilon = 12$ to model the dielectric nature of SiO₂. The simulation was run over a frequency range from approximately 900 cm⁻¹ to 1200 cm⁻¹, in line with previous simulations¹².

Spectroscopy simulations for SiC were modeled after analytical results produced by the finite-dipole model¹³, following the equation

$$\epsilon(\omega) = \epsilon_{\infty} + \frac{\epsilon_{\infty}(\omega_{LO}^2 - \omega_{TO}^2)}{\omega_{LO}^2 - \omega^2 - i\gamma\omega} \text{ (Equation 12)}^{13}$$

with the parameters $\epsilon_{\infty} = 6.56$, $\omega_{LO} = 971$ cm⁻¹, $\omega_{TO} = 797$ cm⁻¹, and $\gamma = 6.6$ cm⁻¹ for SiC¹³. Spectroscopy was run across a frequency range of approximately 890 cm⁻¹ to 950 cm⁻¹, consistent with previous studies¹³.

Microscopy simulations were run in comparison to previous experimental and simulated results for plasmonic modes in gold nanodisks⁹ and polaritonic modes in hBN^{7,8}. Microscopy results were also produced for normal and cancerous human breast cells, with the desire of visualizing optical contrasts between the cells.

Microscopy simulation of plasmonic modes was modeled after previous simulations using the boundary element method⁹. Two plasmonic modes were tested: one for a strong coupling regime, in which both tip and sample were metallic in nature, and one for a weak coupling regime, in which the tip was dielectric in nature, in line with previously simulated modes⁹. The tip was simulated to have a radius of 32 nanometers, with a dielectric constant ϵ of $-10 + 19i$ for the strong coupling regime and a constant of 1.5 for the weak coupling regime, in line with previous simulations⁹. The incident light was simulated using a wavelength of 633 nm⁹.

Microscopy simulations of polaritonic modes in hBN were modeled after previous experimental and simulated results^{7,8}. Simulations were run for both phonon polaritons in a triangular sample⁷ and hyperbolic surface polaritons in a rectangular sample⁸. The dielectric response of hBN was modeled using the equation

$$\epsilon(\omega) = \epsilon_{\infty\mu} + \frac{\epsilon_{\infty\mu}(\omega_{LO,\mu}^2 - \omega_{TO,\mu}^2)}{\omega_{LO,\mu}^2 - \omega^2 - i\omega\Gamma_{\mu}} \text{ (Equation 13)}^{23}$$

with μ denoting either the in-plane or out-of-plane response²³; as I was interested in the scattered response, I chose the out-of-plane parameters for hBN. The parameters for the out-of-plane response were given by $\omega_{LO} = 1610$ cm⁻¹, $\omega_{TO} = 1367$ cm⁻¹, and $\Gamma = 5$ cm⁻¹²³, with $\epsilon_{\infty} = 4.87$ ²⁴. To simulate hyperbolic

surface polaritons, a 1200 nm x 1200 nm sample was simulated at a frequency of 1425 cm⁻¹⁸; for phonon polaritons, triangular samples were simulated at 1550 cm⁻¹⁷.

Microscopy simulations were then run for breast cancer cells, in comparison with normal human cells. The aim of this simulation was to determine whether s-SNOM could discern a noticeable optical contrast between normal and cancerous cells. Cells were approximated as hexagonal disks to reduce computation time and to approximate a circular structure, with a simulated radius of approximately 600 nm. Two cells were separated by approximately 100 nm, one normal and one cancerous, in order to visualize contrasts between the cells. The dielectric response of cells were modeled using the equation

$$\varepsilon(\omega) = \varepsilon_{\infty} + \frac{\omega\tau_1\Delta\varepsilon_1 + \Delta\varepsilon_2}{1 + (i\omega\tau_1)^{\alpha}} + \frac{\Delta\varepsilon_3}{1 + i\omega\tau_2} + \frac{\sigma}{i\omega}$$

(Equation 14)^{4,5}

which accounts for varying amounts of water and compounds within cancerous and normal human cells^{4,5}. For normal human cells, ε_{∞} was set to 2.61, $\Delta\varepsilon_1$ was set to 21.75, $\Delta\varepsilon_2$ was set to -1.84, $\Delta\varepsilon_3$ was set to .99, σ was set to 2.89, τ_1 was set to 2.85 ps, τ_2 was set to .13 ps, and α was set to 1.80⁵; for cancerous cells, ε_{∞} was set to 3.15, $\Delta\varepsilon_1$ was set to 545.6, $\Delta\varepsilon_2$ was set to 2.82, $\Delta\varepsilon_3$ was set to 1.34, σ was set to 7.89, τ_1 was set to 4.67 ps, τ_2 was set to .10 ps, and α was set to 1.90⁵. Simulations were run at 1.8 THz⁵.

3. Results and Discussion

3.1 Spectroscopy

Simulation results demonstrated good quantitative fit with experimental, numerical, and analytical results. This fit is most pronounced in spectroscopy results for SiO₂ (**Figure 6b**), which demonstrates an almost perfect match with analytical point-dipole¹⁴ and previously calculated experimental and numerical results¹². Spectroscopy results for

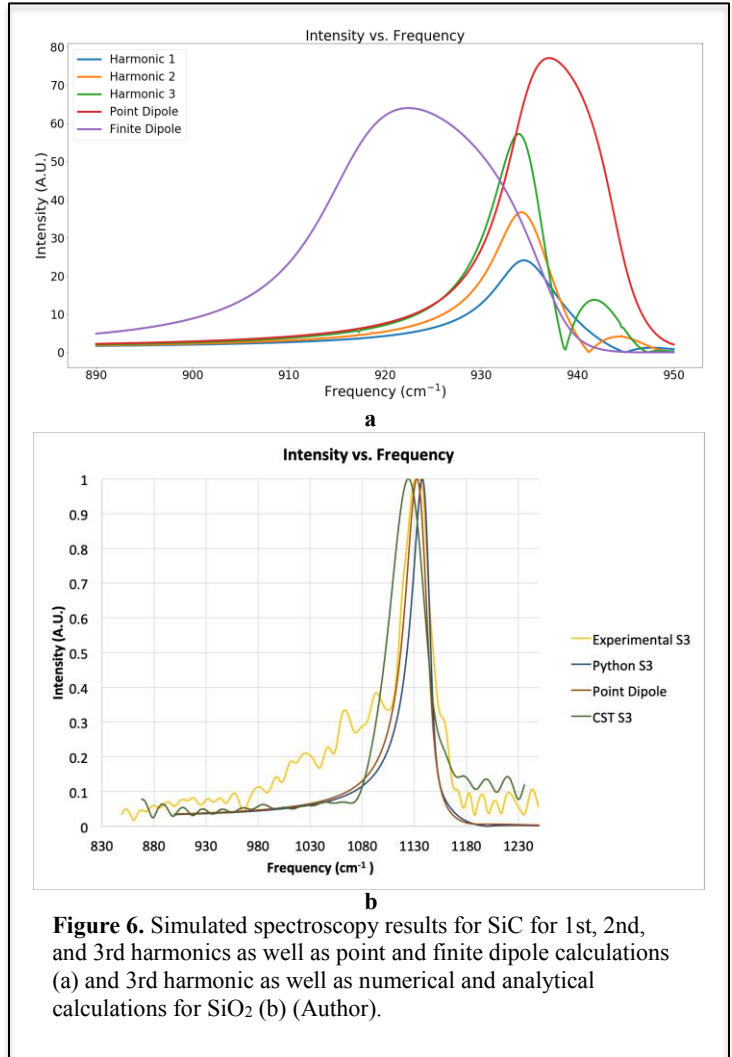


Figure 6. Simulated spectroscopy results for SiC for 1st, 2nd, and 3rd harmonics as well as point and finite dipole calculations (a) and 3rd harmonic as well as numerical and analytical calculations for SiO₂ (b) (Author).

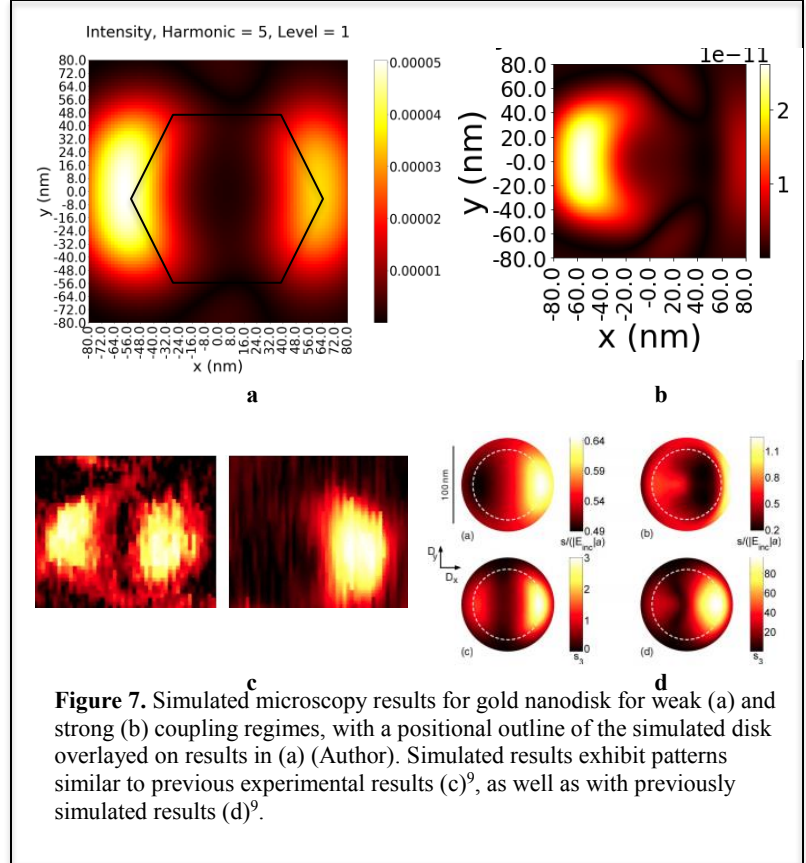
SiC (**Figure 6a**) show more discrepancy from point-dipole and finite-dipole¹³ accuracy, as the peak intensity occurs at about 935 cm^{-1} , rather than the 940 cm^{-1} and 920 cm^{-1} calculated by the point and finite dipole models, respectively. These slight discrepancies between the calculated DDA spectrums and the analytical and numerical results may be attributed to slight inaccuracies in the mathematical terms used to portray the image spheres representing the substrate, which interact differently with real and other image spheres, within the interaction matrix than terms used for purely real spheres. Currently, this issue has yet to be resolved.

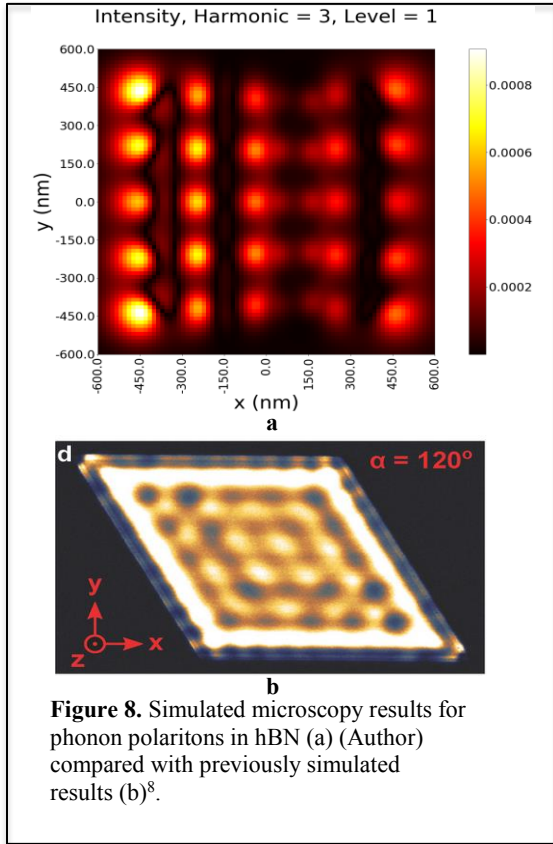
3.2 Simulated Plasmonic and Polaritonic Modes

Plasmon Modes in Gold Nanodisks

Plasmon modes were simulated to great accuracy in both the strong and weak coupling regimes (**Figure 7a, 7b**). Simulated patterns matched existing simulated and experimental results⁹ (**Figure 7c, 7d**); in previous results, weak coupling regimes demonstrated two fringes of bright intensity at the edges of the nanodisk, while strong coupling regimes demonstrated a single fringe at a single edge of the nanodisk (**Figure 7c, 7d**)⁹; this was demonstrated by my own simulation (**Figure 7a, 7b**).

Thus, this demonstrated the applicability of the DDA simulation to the imaging of plasmonic modes in gold nanodisks.





a pattern that differed greatly from previously simulated interference patterns⁷ (**Figure 9b**), which may also be attributed to failure of the iterative solver to converge, as well as discrepancies within the mathematical terms of the interaction matrices. Ongoing work utilizing different solvers for DDA or creating a theoretical framework properly considering image spheres is expected to resolve these issues.

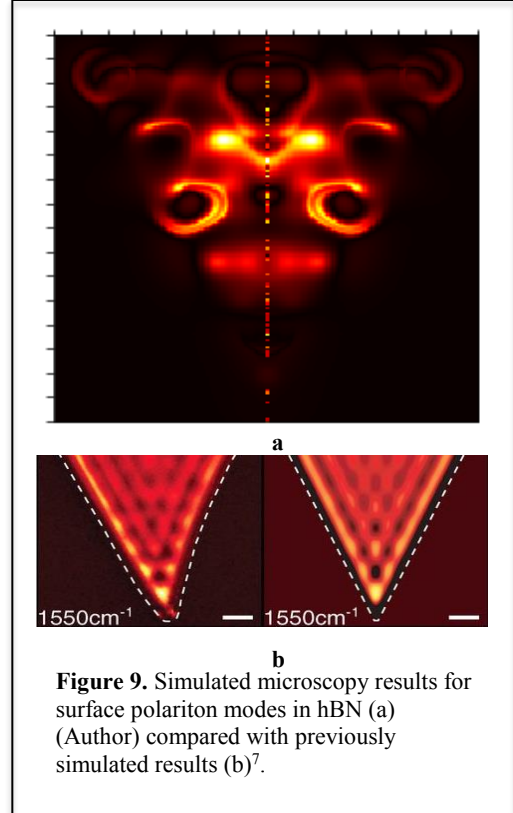
3.3 Optical Contrasts Between Cancerous and Normal Human Breast Cancer Cells

Optical contrasts were successfully simulated between normal and cancerous human cells (**Figure 10a, 10b**). Optical intensity of the human cells were nearly six

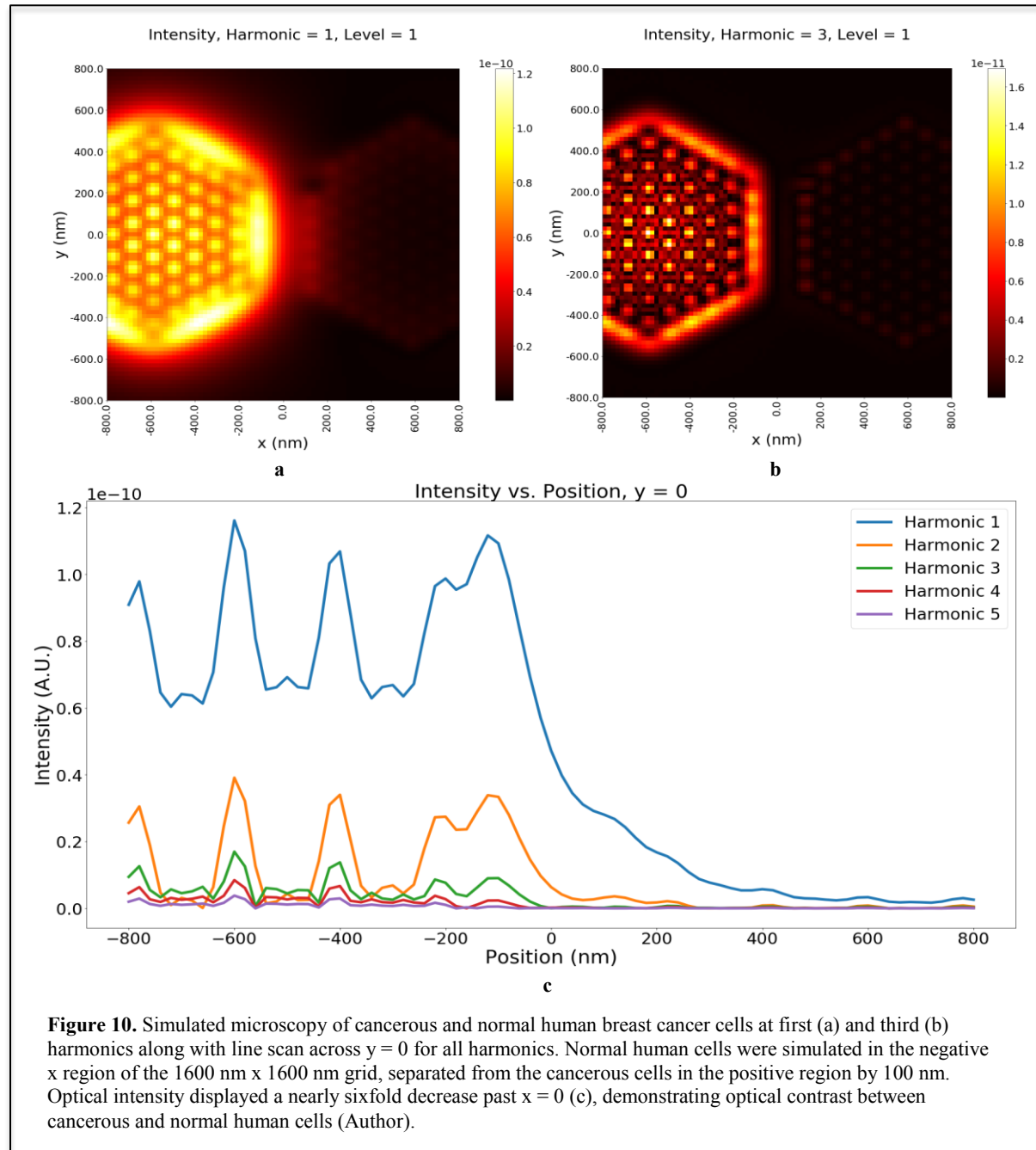
Hyperbolic surface polaritons were simulated in hBN in a rectangular sample. Simulated results demonstrated an interference pattern with bright fringes at the outer edges of the sample (**Figure 8a**); this was consistent with the previous experimental results⁸, which demonstrated similar interference patterns⁸ (**Figure 8b**). Thus, DDA was able to simulate the interference patterns created by hyperbolic surface polaritons⁸, validating its applicability to s-SNOM and polariton imaging.

Not all polariton patterns were successfully simulated, due to both convergence issues with the iterative solver and the previously mentioned issues with the formulation for the DDA interaction matrix. A simulated pattern for phonon polaritons in hBN (**Figure 9a**)

showed



times as large as the simulated cancer cells (**Figure 10c**), demonstrating the desired contrast; this is in line with previous mathematical results^{4,5}, which predicted significant optical differences between human and cancer cells^{4,5}. Since breast cancer cells have higher water content than normal human cells^{4,5}, the optical response for cancerous cells was expected to be less intense, as the water content causes greater absorption of light^{4,5}. This was shown in the simulated results (**Figure 10**).



3.4 Limitations

Discrepancies from expected results were seen in both microscopy and spectroscopy (**Figures 6a, 9a**), due to both convergence issues with the solver used and inaccuracies within the interaction matrix. The iterative solver used in the implementation was unable to accurately converge, possibly due to upper bounds set by the solver. Other methods could potentially solve these convergence issues, including the fast Fourier transform (FFT) method, which has previously been applied to DDA^{16,17,18}. In the case of image spheres, the exact interaction between simulated dipoles and their corresponding images in the substrate are unclear. Future studies should investigate the relationship between image spheres and other simulated spheres, as well as the interaction between images and corresponding real spheres, to clarify the interactions between simulated spheres. In addition, to increase the accuracy of microscopy simulations, the number of dipole spheres used in simulation may be increased^{16,17,18}.

4. Conclusion

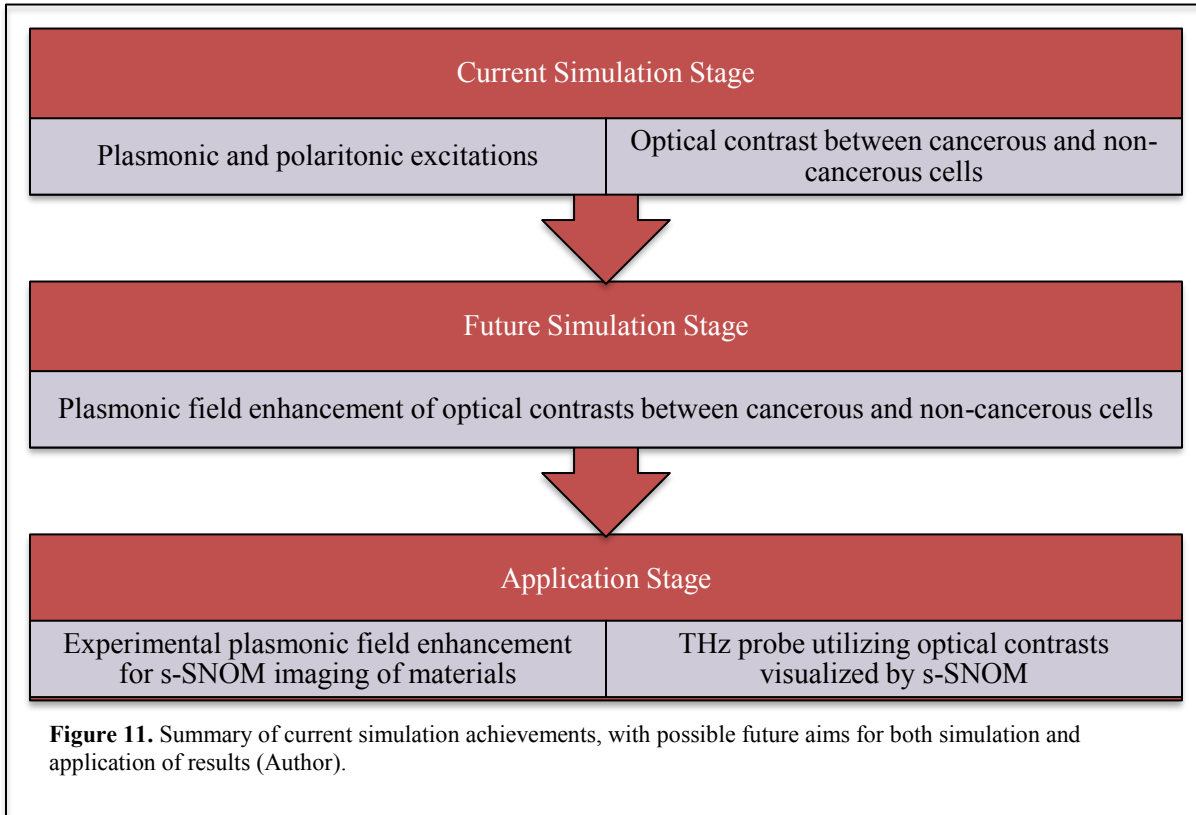
Simulated results (**Figures 6b, 7a, 7b, 8a, 10a, 10b, 10c**), utilizing the DDA, successfully reproduced previous experimental and simulated images of plasmonic and polaritonic excitations in various materials^{8,9} (**Figures 7c, 7d, 8b**), as well as optical contrasts between normal and cancerous breast cancer cells in the THz regime^{4,5}. Slight discrepancies between simulated and previous results (**Figures 6a, 9a**) may be attributed to the inability of the iterative solver to converge, as well as inaccuracies within the interaction matrices describing the interaction between the approximated spheres and their images.

Given more time, I would focus on refinement of the DDA for such simulations, particularly for the interaction matrices describing the interactions between real and image spheres. I would then use the DDA simulation method to predict possible plasmon or polariton patterns in various materials, such as gold, hBN, and graphene⁶, and particularly at THz frequencies, in which s-SNOM imaging is riddled with difficulties arising from high signal-to-noise ratios¹. Further knowledge of these patterns would allow for better applications to optics, such as controlled polaritonic light transport and plasmonic sensing⁶.

Furthermore, as this novel simulation method has shown to be applicable to plasmonic excitations and biological cell contrasts, I would study the possible improvement of biological imaging through plasmonic field enhancement, which has previously been shown to be able to enhance optical signals by several orders of magnitude²⁵. Developing plasmonic field enhancement may enhance optical contrasts between cancer and human cells, improving the ease of cancer diagnosis by making normal human cells more optically distinguishable from cancerous ones. Moreover, the ability of s-SNOM to create visual contrast between cancerous and non-cancerous cells allows for the possibility of constructing non-invasive optical probes for cancer diagnosis, especially in the THz regime. Such a probe would allow for

efficient and effective cancer diagnosis without the need for potentially harmful imaging methods, such as X-rays^{2,3}.

A summary of results of this paper are shown in **Figure 11**. The simulation of s-SNOM imaging has been achieved through the usage of DDA, and has been shown to be applicable to plasmonic and polaritonic excitations, as well as to discerning optical contrasts between cancerous and non-cancerous cells in the THz regime. Future studies should focus on the usage of plasmonic field enhancement to magnify this contrast, which could lead to the experimental and practical usage of such imaging methods in cancer diagnosis, potentially through a non-invasive probe utilizing THz imaging. In addition, plasmonic field enhancement could potentially be used in s-SNOM imaging to help discern the optical properties of SCQMs, allowing for the study of materials, such as Mott insulators and high-temperature superconductors^{1,11}. These DDA simulations have, therefore, been shown to be a powerful and promising method for s-SNOM imaging of various materials, and holds great potential for applications in the fields of physics and biology.



References

- [1] Chen, X., Hu, D., Mescall, R., You, G., Basov, D. N., Dai, Q., & Liu, M. (2019). Modern Scattering-Type Scanning Near-Field Optical Microscopy for Advanced Material Research [PDF]. *Advanced Materials*.
- [2] Yang, X., Zhao, X., Yang, K., Liu, Y., Liu, Y., Fu, W., & Luo, Y. (2016). Biomedical Applications of Terahertz Spectroscopy and Imaging [PDF]. *Trends in Biotechnology*. <https://doi.org/10.1016/j.tibtech.2016.04.008>
- [3] Yu, C., Fan, S., Sun, Y., & Pickwell-MacPherson, E. (2012). The potential of terahertz imaging for cancer diagnosis: A review of investigations to date [PDF]. *Quantitative Imaging in Medicine and Surgery*. <https://doi.org/10.3978/j.issn.2223-4292.2012.01.04>
- [4] Truong, B. C. Q., Tuan, H. D., Fitzgerald, A. J., Wallace, V. P., & Nguyen, H. T. (2015). A Dielectric Model of Human Breast Tissue in Terahertz Regime [PDF]. *IEEE Transactions on Biomedical Engineering*. <https://doi.org/10.1109/TBME.2014.2364025>
- [5] Truong, B. C. Q., Tuan, H. D., Fitzgerald, A. J., Wallace, V. P., Nguyen, T. N., & Nguyen, H. T. (2015). Breast Cancer Classification Using Extracted Parameters from a Terahertz Dielectric Model of Human Breast Tissue [PDF]. *Conference Proceedings - IEEE Engineering in Medicine and Biology Society*. <https://doi.org/10.1109/EMBC.2015.7318974>
- [6] Basov, D. N., Fogler, M. M., & Garcia de Abajo, F. J. (2016). Polaritons in van der Waals materials. *Science*. <https://doi.org/10.1126/science.aag1992>
- [7] Dai, S., Fei, Z., Ma, Q., Rodin, A. S., Wagner, M., McLeod, A. S., . . . Basov, D. N. (2019). Tunable Phonon Polaritons in Atomically Thin van der Waals Crystals of Boron Nitride. *Science*. <https://doi.org/10.1126/science.1246833>
- [8] Dai, S., Tymchenko, M., Yang, Y., Ma, Q., Pita-Vidal, M., Watanabe, K., . . . Basov, D. N. (2018). Manipulation and Steering of Hyperbolic Surface Polaritons in Hexagonal Boron Nitride. *Advanced Materials*.
- [9] Garcia-Etxarri, A., Romero, I., Garcia de Abajo, F. J., Hillenbrand, R., & Aizpurua, J. (2009). Influence of the tip in near-field imaging of nanoparticle plasmonic modes: Weak and strong coupling regimes. *Physical Review B*, 79. <https://doi.org/10.1103/PhysRevB.79.125439>
- [10] Hillenbrand, R., & Keilmann, F. (2001). Optical oscillation modes of plasmon particles observed in direct space by phase-contrast near-field microscopy. *Applied Physics B*. <https://doi.org/10.1007/s003400100656>
- [11] Liu, M., Sternbach, S. J., & Basov, D. N. (2017). Nanoscale electrodynamics of strongly correlated quantum materials. *Reports on Progress in Physics*. <http://dx.doi.org/10.1088/0034-4885/80/1/014501>
- [12] Chen, X., Fan Bowen Lo, C., Zheng, W., Hu, H., Dai, Q., & Liu, M. (2017). Rigorous numerical modeling of scattering-type scanning near-field optical microscopy and spectroscopy [PDF]. *Applied Physics Letters*. <https://doi.org/10.1063/1.5008663>
- [13] Cvitkovic, A., Ocelic, N., & Hillenbrand, R. (2007). Analytical model for quantitative prediction of material contrasts in scattering-type near-field optical microscopy. *Optics Express*. <https://doi.org/10.1364/OE.15.008550>
- [14] Knoll, B., & Keilmann, F. (2000). Enhanced dielectric contrast in scattering-type scanning near-field optical microscopy. *Optics Communications*.
- [15] Purcell, E. M., & Pennypacker, C. R. (1973). Scattering and Absorption of Light by Nonspherical Dielectric Grains. *The Astrophysical Journal*.
- [16] Draine, B. T. (1988). The Discrete-Dipole Approximation and its Application to Interstellar Graphite Grains. *The Astrophysical Journal*.

- [17] Draine, B. T., & Flatau, P. J. (1994). Discrete-dipole approximation for scattering calculations. *Journal of the Optical Society of America A*.
- [18] Yurkin, M. A., & Hoekstra, A. G. (2007). The discrete dipole approximation: An overview and recent developments. *Journal of Quantitative Spectroscopy & Radiative Transfer*.
<https://doi.org/10.1016/j.jqsrt.2007.01.034>
- [19] Loke, V. L. Y., & Mengüç, M. P. (2010). Surface waves and atomic force microscope probe-particle near-field coupling: discrete dipole approximation with surface interaction. *Journal of the Optical Society of America A*. <https://doi.org/10.1364/JOSAA.27.002293>
- [20] Ruan, Y., Li, K., Lin, Q., & Zhang, T. (2018). Tip-Nanoparticle Near-Field Coupling in Scanning Near-Field Microscopy by Coupled Dipole Method. *Chinese Physics Letters*. Retrieved from <https://iopscience.iop.org/article/10.1088/0256-307X/35/4/044203/meta>
- [21] Juluri, B. K. (2016). Coupled Dipole Approximation in Python. Retrieved from <http://juluribk.com/2016/07/20/coupled-dipole-approximation-in-python/>
- [22] Xu, S. (n.d.). [Code for Simulated Spheres and Demodulation]. Unpublished raw data.
- [23] Dai, S., Fei, Z., Ma, Q., Rodin, A. S., Wagner, M., McLeod, A. S., . . . Basov, D. N. (2019). Supplementary Materials for Tunable Phonon Polaritons in Atomically Thin van der Waals Crystals of Boron Nitride. *Science*. <https://doi.org/10.1126/science.1246833>
- [24] Cai, Y., Zhang, L., Zeng, Q., Cheng, L., & Xu, Y. (2007). Infrared reflectance spectrum of BN calculated from first principles [PDF]. *Solid State Communications*.
<https://doi.org/10.1016/j.ssc.2006.10.040>
- [25] Ciraci, C., Hill, R. T., Mock, J. J., Urzhumov, Y., Fernández-Domínguez, A. I., Maier, S. A., . . . Smith, D. R. (2019). Probing the Ultimate Limits of Plasmonic Enhancement [PDF]. *Science*.
<https://doi.org/10.1126/science.1224823>